Nuclear Instruments and Methods in Physics Research A307 (1991) 220–230
North-Holland

# The honeycomb strip chamber: the application in LHC/SSC experiments and the test results of a prototype

Harry van der Graaf [a], Joop Buskens [a], Gerard Faber [b], Adriaan König [c], Paul Rewiersma [a] and Thei Wijnen [c]

[a] *NIKHEF-H, Kruislaan 409, 1098 SJ Amsterdam, The Netherlands*
[b] *Now at ETH / CERN, Zürich / Geneva, Switzerland*
[c] *University of Nijmegen and NIKHEF, Toernooiveld 1, 6525 ED Nijmegen, The Netherlands*

Received 5 June 1991

The honeycomb strip chamber (HSC) is a new position sensitive detector. It consists of a stack of folded foils, forming a rigid honeycomb structure. In the centre of each hexagonal cell a wire is strung. Conducting strips on the foils, perpendicular to the wires, pick up the induced avalanche charge. Test results of a prototype show that processing the signals from three adjacent strips nearest to the track gives a spatial resolution better than 64 μm for perpendicular incident tracks. The chamber performance is only slightly affected by a magnetic field.

## 1. Introduction

Experiments at the future LHC or the SSC facilities face a very high event rate due to the required luminosity. The bunch rate (66.6 and 62.5 MHz respectively) is very high. Moreover, at maximum luminosity, some 40 events are expected for each bunch crossing. The high radiation level limits the choice of materials to be applied in such a detector. The design of detectors is therefore a complex affair.

Monte Carlo simulations show, however, that the exclusive detection of muons may well enable the discovery of, for instance, a Higgs particle, assuming that some of its decay channels will imply the creation of one or more $Z^0$ particles which decay with a specific probability in muons. A four-muon event is, for instance, well recognisable on top of the background [1–3].

Muons are relatively easy to detect: hadrons, photons and electrons can be absorbed in calorimeters. Outside the calorimeters the muon count rate, including muons created in the decay of pions in the calorimeter, and the contribution due to punch through particles, will be of the order of 10 MHz for a hermetic detector.

The measurement of the momentum of the muons provides information about the origin of the muons and the process in which they were created. The muon momentum is obtained from the measurement of its track curvature in a magnetic field. The required precision of this measurement is at present a matter of controversy. The natural width of the $Z^0$ resonance forms a limit to a useful resolution. The momentum resolution depends on the geometry and strength of the magnetic field, the spatial resolution of the muon detector and scattering of the muon against detector material.

Muon detectors are usually drift chambers; the number of track sampling sense wires can be increased if a high precision is required [4]. The strong magnetic field, proposed for some LHC or SSC detectors, can cause problems in the application of accurate drift chambers. Parameters determining the space–time relation must be either accurately known or well controlled (electric field, magnetic field, gas mixing ratio, temperature, pressure). Furthermore, the slow response of drift chambers requires additional trigger detectors like scintillators or resistive plate chambers [5].

In this article we present the honeycomb strip chamber (HSC) as an alternative for drift chambers [6,7].

## 2. Principle

In fig. 1 the basic elements of the chamber are shown: each wire is coaxially surrounded by conducting hexagonal rings. Since the gap between the rings is small, the cell is well comparable to a proportional counting tube. A muon passing through the volume inside the rings results in an avalanche on the wire.

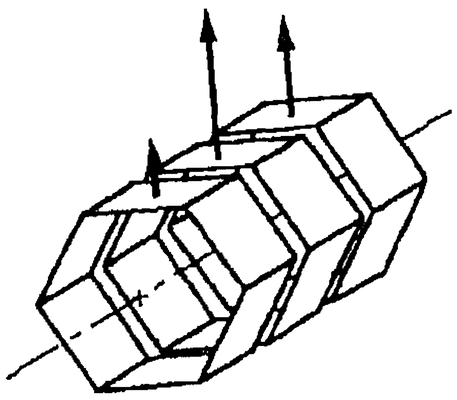

Fig. 1. Principle of the honeycomb strip chamber. The magnitudes of the signals from three adjacent hexagonal rings around the wire are a function of the track position coordinate along the wire.

The negative charge signal from the wires equals the total positive charge signal on the rings at any time. The charge distribution over the rings is an exclusive function of the position of the drifting ion cloud and of the geometry of wires and rings. This is the well known principle used in "segmented cathode strip readout" of MWPCs [8–14].

In fig. 2 the construction element of the chamber is shown: folded foils with conducting strips perpendicular to the fold edges are glued together. A stack of these foils is a stiff, rigid and self-supporting honeycomb (see fig. 3). In the centre of each hexagonal cell a wire is strung, the wire tension is held by the cell walls.

The geometry of fig. 3 requires conducting strips at both sides of each foil. As a consequence, the mutual capacitance between a strip [1] and its upper and lower neighbour is very high. Since each strip is virtually grounded by its amplifier, the source capacitances are very high and the signal/noise ratio is poor.

This problem is solved in the geometry of fig. 4: each layer of cells is covered with an insulating flat foil which acts as a base for the next layer. Odd and even planes are relatively shifted by half a cell pitch. In this geometry the "vertical" capacity is much smaller than the unavoidable capacitance between horizontally neighbouring strips. The interconnecting plane between two neighbouring cells is as small as mechanically possible, minimizing the insensitive surface.

[1] A strip is defined here as a group of interconnected hexagonal rings.

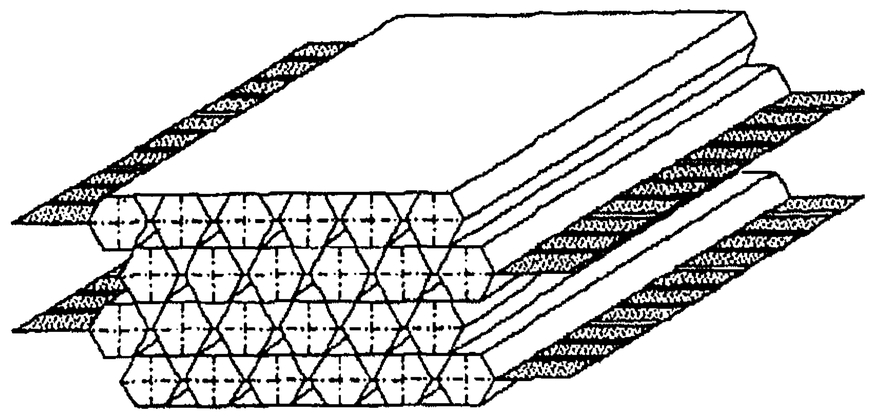

Fig. 4. Structure with plane foils between cell layers.

## 3. Simulation

In order to study the relation between the spatial resolution and parameters like the chamber geometry,

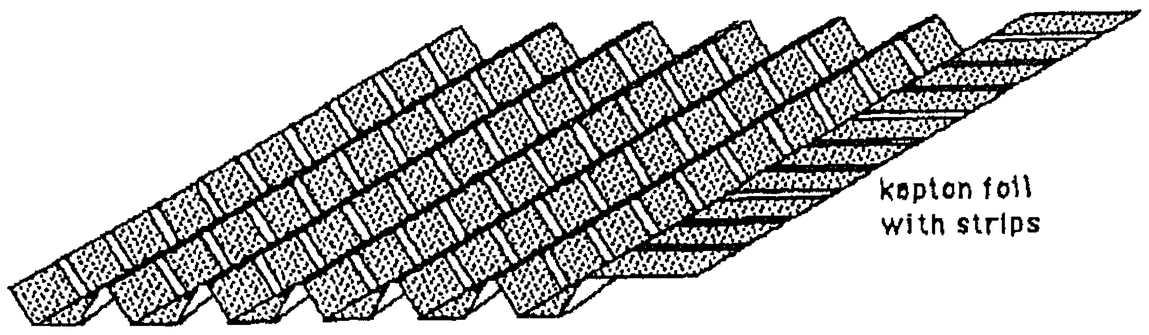


Fig. 2. Chamber construction. Two folded foils, fixed together, form a layer of honeycomb cells.

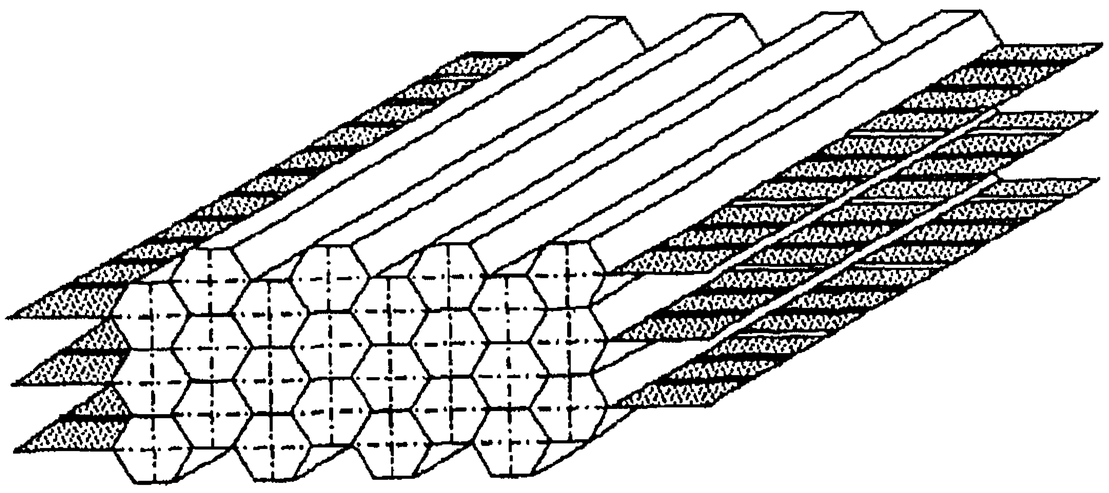

Fig. 3. Honeycomb structure. Strip readout for each cell is not possible because of the too large capacitance between the strips. The structure is, however, a good replacement for straw tubes.

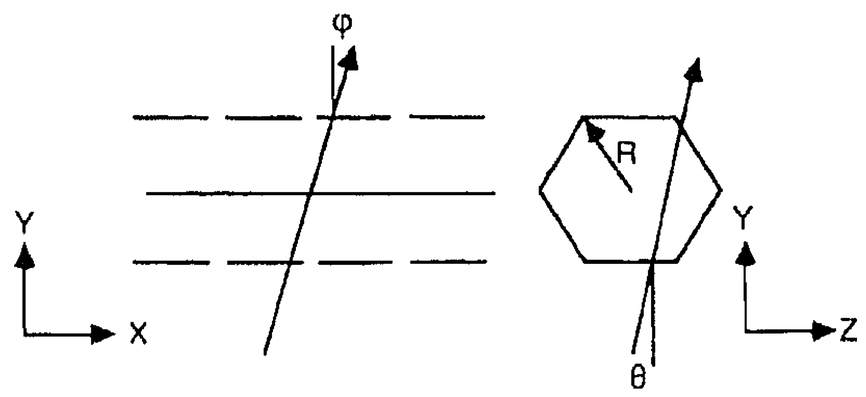


Fig. 5. Coordinate system and nomenclature.

the gas mixture and the angle of incidence of the particle, a Monte Carlo simulation program was written. It had the following sequence:

- generate a track with angles $\phi$ and $\theta$ through a cell (see fig. 5); calculate its crossing points with the cell walls;
- generate the points where a primary ion–electron pair is created, given the probability per unit length that it occurs [15];
- generate the energy of the released primary electron, assuming the Rutherford energy distribution [16];
- calculate the number of secondary electrons in the cluster released by the (energetic) primary electron [18]; calculate the position of the centre of gravity of this cluster using the angle of emission and the calculated range;
- calculate the change in the centre of gravity of each cluster due to diffusion;
- generate an avalanche for each cluster; include the Curran fluctuations in the gas gain [19].
- calculate the $X$ coordinate of the centre of gravity of all electrons created in the avalanche;
- calculate the charges on three nearest hexagonal rings, given the strip charge distribution function (see appendix A);
- superimpose Gaussian preamplifier noise on the charge signals;
- calculate the "measured" centre of gravity of the track; store the difference with the real track position in a histogram.

Let us assume that the integration time constant of the strip electronics is large compared with the maximum drift time of the secondary electrons. The charge signals on wires and strips can thus be regarded as a superposition of all distributions due to the avalanches caused by the individual secondary electrons. As a result we measure the $X$ coordinate of the centroid of the positive ions, and therefore the $X$ coordinate of the centroid of the secondary electrons (neglecting Curran fluctuations). The results of the Monte Carlo simulation are therefore presented in the form of centroid distributions.

In fig. 6 the centroid distribution in the $X$ direction (along the wire) of the secondary electrons is shown for perpendicular incident muons just after the muon passage: diffusion effects are omitted. The distribution is determined by the energy distribution of δ-rays. In the calculation only the interaction of the muon with the gas was taken into account; the emission of (partly absorbed) δ-rays by the foils has not been taken in account. High energy δ-rays have a long range and cause a large error in the measured track position. From fig. 6 one can see that the probability of a 20 μm error in the measurement of a track position is less than 1%. These measurements can be rejected by pulse height discrimination and cuts on extreme position samples.

The diffusion of electrons during their drift towards the anode wire was approximated by taking the superposition of the contributions from each cluster:

$$\sigma_x = D\frac{\sqrt{R_d}}{\sqrt{n}},$$

where $\sigma_x$ equals the width of the distribution in the $X$ direction of the secondary electrons in a cluster associated with one δ-ray at the moment of arrival at the anode wire. The transverse diffusion constant $D$ for Ar gas was fixed at 0.1 $\sqrt{\text{mm}}$ [20]; $R_d$ is the drift path between the cluster and the anode wire; $n$ equals the number of electrons in the cluster. Fig. 7 shows the width of Gaussian fits to the centroid distributions for different values of the distance $Z$ between the track and the wire. The secondary electrons created by tracks

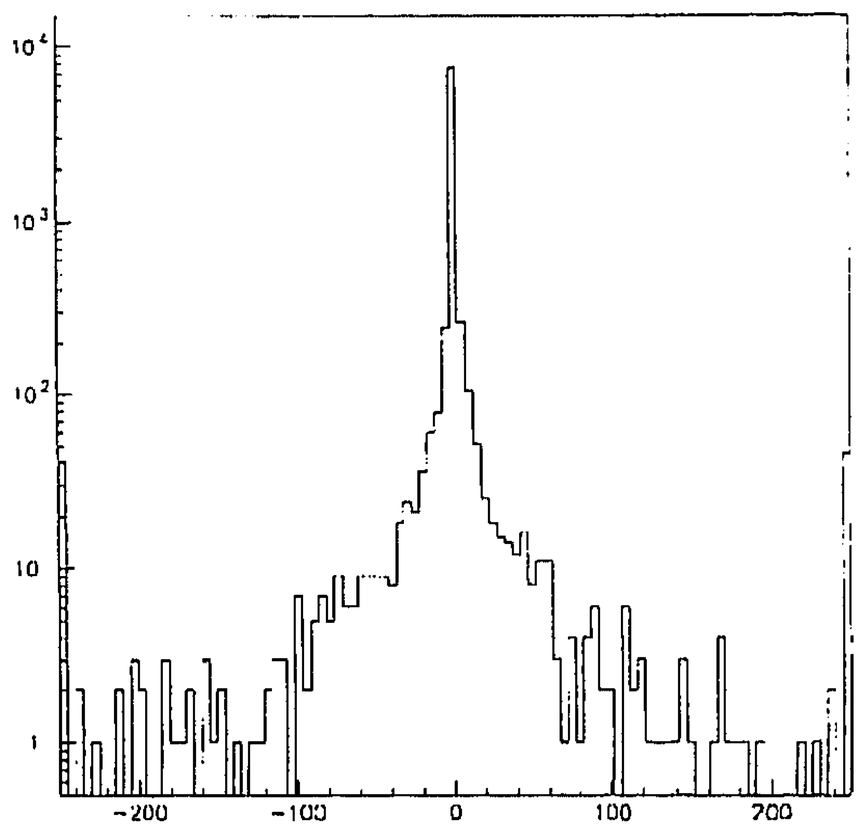


Fig. 6. Distribution of the secondary electrons centroid for $\phi = 0$ rad, not regarding diffusion effects. The distribution is determined by the range of δ-rays.

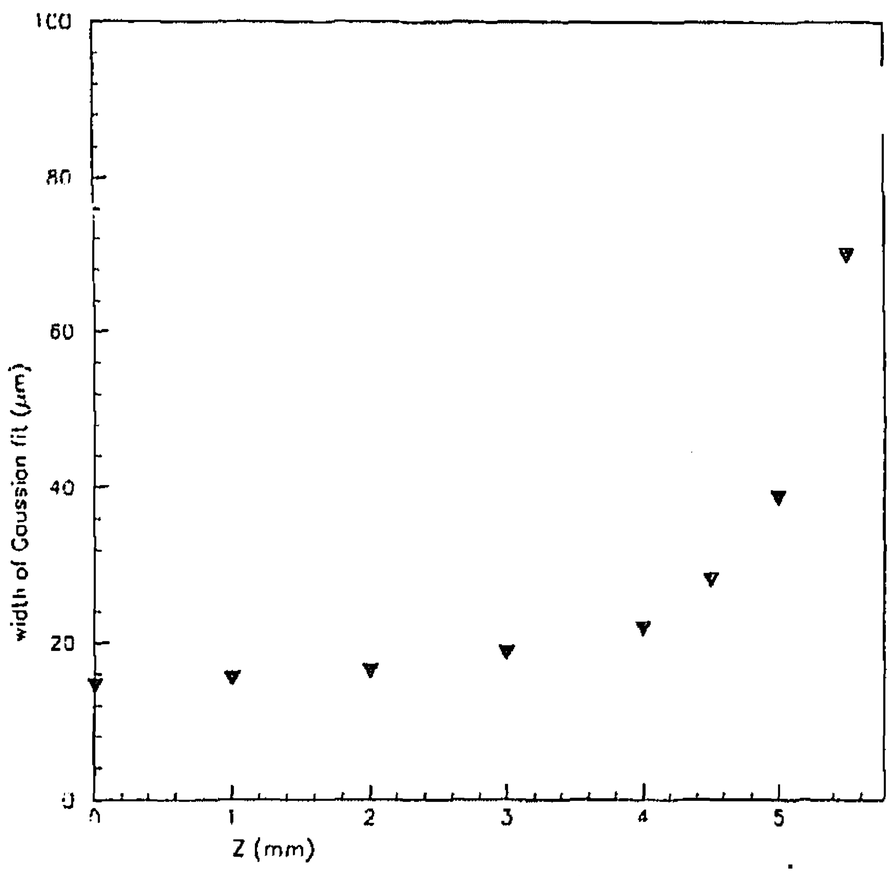


Fig. 7. Distribution width of the secondary electrons centroid due to diffusion as a function of $Z$, being the distance between the track and the wire. The distribution gets wider for large $Z$ because of the larger average drift path and the smaller number of secondary electrons.

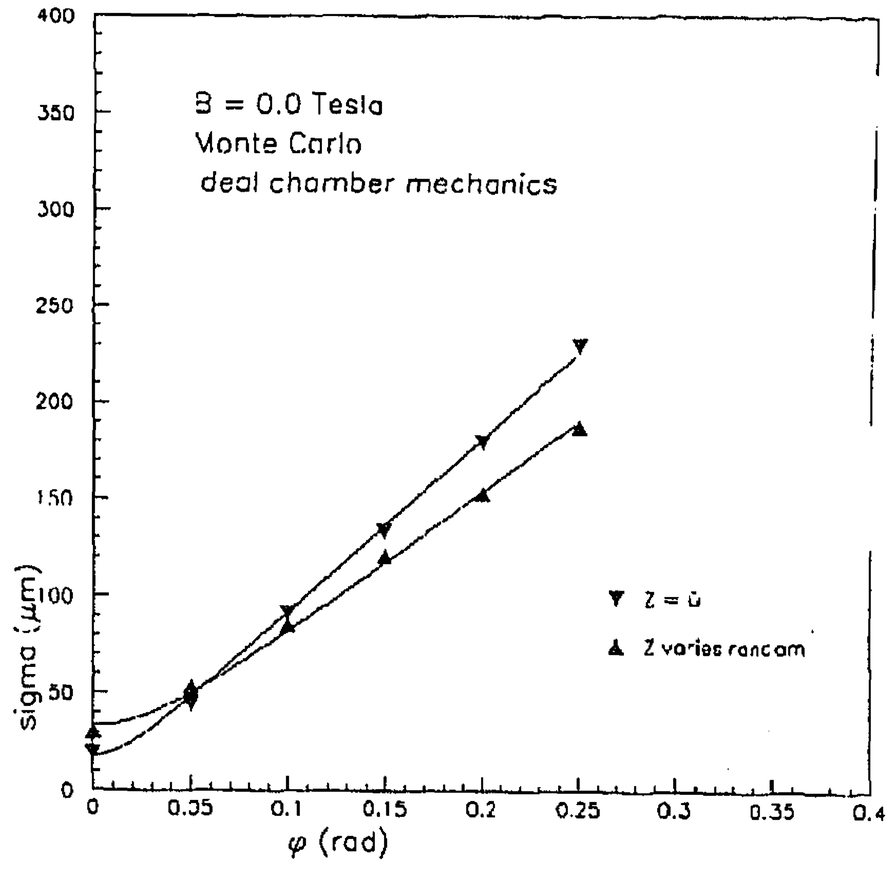


Fig. 8. The width of the distribution of the secondary electron centroid as a function of $\phi$. The widening is due to the statistical fluctuations in the density along the track of the secondary electrons. One curve is shown for $Z = 0$; the second curve is the result of a random homogeneous distribution $|Z| < R$. Gas: Ar.

close to the wire ($Z = 0$) have all possible distances to the anode wire, up to the cell radius. Mainly electrons from the region near the cathode contribute to the increase in the width due to diffusion. For tracks further away from the wire the width increases because a) the average drift path is longer and b) the number of participating clusters is smaller.

Fig. 8 shows the width of the centroid distribution of the secondary electrons as a function of angle $\phi$; the diffusion effect and the Curran fluctuations are included. For a mechanically ideal chamber equipped with perfect electronics the spatial resolution would be equal to the width values shown. We will approximate the ultimate spatial resolution of a honeycomb cell as:

$$\sigma^2 = \sigma_0^2 + (\sigma_\phi \phi)^2.$$

The best spatial resolution $\sigma_0$ is obtained for normal incident tracks ($\phi = 0$) and is determined by the diffusion of the drifting electrons. For larger $\phi$ the Poisson statistics in the random distribution of points of primary interaction between the muon and the gas degrades the resolution: the term $(\sigma_\phi \phi)$ takes this into account. The value of the constant $\sigma_\phi$ is roughly proportional to the track length within the cell, and therefore proportional to the cell radius. For tracks further away from the wire ($|Z| > \frac{1}{2}R$) the track length decreases: the degradation of the resolution with $\phi$ is less. The value of $\sigma_\phi$ is 900 μm and 750 μm respectively for tracks through the central region of the cell and for tracks where the $Z$ coordinate varies randomly, as is shown in fig. 8. The contribution of Curran fluctuations to the given values for $\sigma_\phi$ is about 10%. If Xe gas is used, the value for $\sigma_\phi$ can be as low as 400 μm for muons with an energy well in the area of the relativistic rise.

In order to establish signal/noise ratio demands, a gas gain of $10^5$ was assumed; fixing the rms of the equivalent noise of the preamplifiers at 7000 electrons, a spatial resolution of 100 μm is obtained for $|\phi| < 0.1$ rad. The optimum in the strip pitch tallied with a previous calculation [21,22].

The allowed equivalent noise limits the length of the strips; a high gas gain may allow strip lengths up to a few meters. The maximum length of a chamber may be twice the maximum strip length by breaking the strips in the chamber center and applying readout circuitry at opposite strip ends.

## 4. The prototype, the readout system and the experimental setup

The encouraging results of the Monte Carlo simulation led us to decide to construct a small HSC. We gained experience in folding and glueing of foil. Small tolerances in the cell geometry, the strip width and the strip pitch were realised, enabling a comparison of the chamber performance with the Monte Carlo predictions.

The geometry of the chamber is shown in fig. 9. It consisted of ten layers; the outer layers had a mere shielding function. In the cells of the eight central planes gold plated tungsten wires (diameter: 20 μm) were strung in the cell axis.

Kapton foils with Cu strips were commercially obtained. Tolerances on strip position and strip width were better than 100 μm. Each chamber layer consisted of 24 cells and 54 strips.

At the open ends of the cells an aluminium end plate was glued; nylon plugs, fitting in the chamber cells as well as in holes in the end plate defined the position of the cell walls. An aluminium cover plate formed a sealed gas distribution box with the end plate. The cover plate was equipped with shrinking tubes which fixed the wires. The completed chamber was mounted on a solid aluminium plate which acted as a support for the preamplifiers and cables (see fig. 10).

Twelve adjacent wires of each plane were read out: after a hybrid preamplifier [23] and discriminator (LeCroy MVL 407) the 96 digital signals were transported along 40 m twisted pairs cables to the CAMAC TDCs (LeCroy 4290) in the counting room.

Strip signals (128 channels) were amplified by 4-channel hybrid charge amplifiers [23] and transported to the counting room. Here the signals were filtered, amplified and converted into monopolar signals using "analog line receivers" [23]. These ALRs were 16 channel NIM modules. The output signals were fed into gated, charge-sensitive ADCs (LeCroy 2282).

We used the secondary SPS beam X3 of the L3 test site in the West Hall at CERN. The beam consisted of electrons and pions of 10 GeV. The electrons were absorbed by inserting 10 mm Pb; per beam spill up to 500 pions passed through the chamber.

The chamber was placed in the large L3 test beam magnet. The magnetic field had a maximum value of 0.93 T. The trigger was obtained from two hodoscopes and associated electronics. One hodoscope was placed upstream and one downstream from the magnet. Each hodoscope consisted of two scintillators with overlapping surface. The geometry of the overlap had the same dimensions as the sensitive area of the chamber. The fourfold coincidence between the scintillators acted as an efficient trigger with virtually no background.

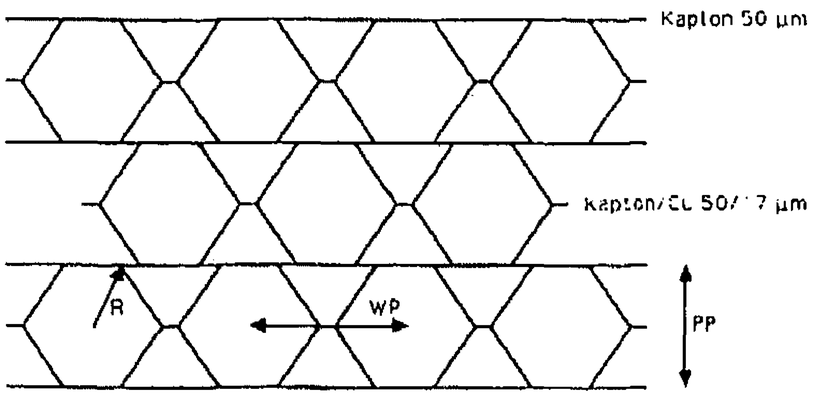


Fig. 9. The geometry of the prototype chamber: cell outer radius $R$: 5.774 mm; wire pitch WP: 13.0 mm; plane pitch PP: 10.7 mm; strip pitch: 5.00 mm; strip width: 4.00 mm.

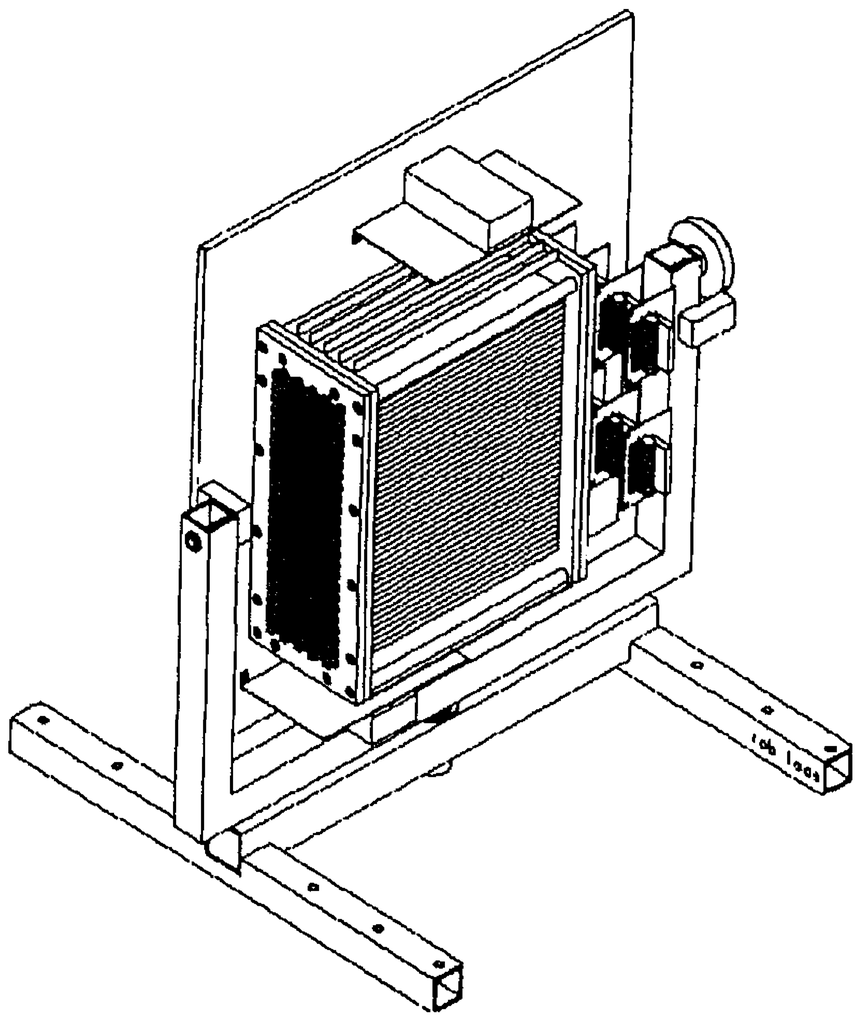

Fig. 10. The chamber support. The angles $\phi$ and $\theta$ could be varied by a rotation of the chamber.

The gas system consisted of simple electronic flow controllers (Brooks 5878); the stability of the mixing rate needed for high-accuracy drift chambers is not required. Since the gas propagates neatly through the honeycomb cells the chamber was operational after flushing twice its volume. The used gas mixtures were: Ar/ethane 60/40, Ar/$CO_2$ 80/20 and Ar/$CO_2$ 50/50.

Positive HV was applied on the wires: the value was adjusted such that the amplitudes of the strip signals were within the ADC range. The values were 1570, 1700 and 1950 V respectively for the gas mixtures given above. This corresponds to a gas gain of about $10^5$.

The honeycomb cell with its central wire form an almost ideal counting tube. The electric field is therefore only strong around the wire. No HV breakdowns occurred during the test; a gas gain of $10^6$ could be maintained.

## 5. Results

For each event the data from 128 ADC channels and 96 TDC channels was written on tape. Fig. 11

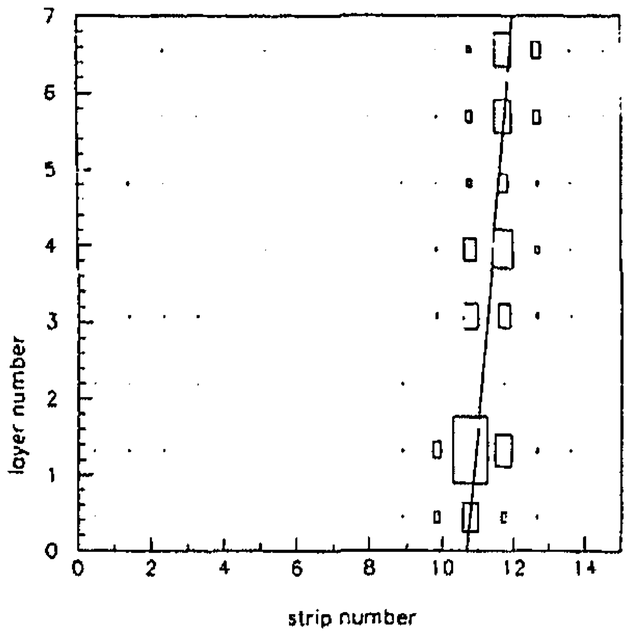


Fig. 11. Strip charges from a track through the 8-layer chamber. The strip charge is proportional with a side of a box. The change in the ratio of the three largest signals, going from one layer to the next, is clearly observable.

shows a typical event. From the TDC data the angle $\theta$, the $Z$ coordinate and the timing of the track can be obtained. Fig. 12 shows drift time distribution for three different gas mixtures. Because of the high level of interference noise, the thresholds of the discriminators had to be set rather high. The recorded drift times are therefore disturbed by the fluctuation of individual pulse heights; no further analysis of the $Z$ coordinate and angle $\theta$ of the track has been done.

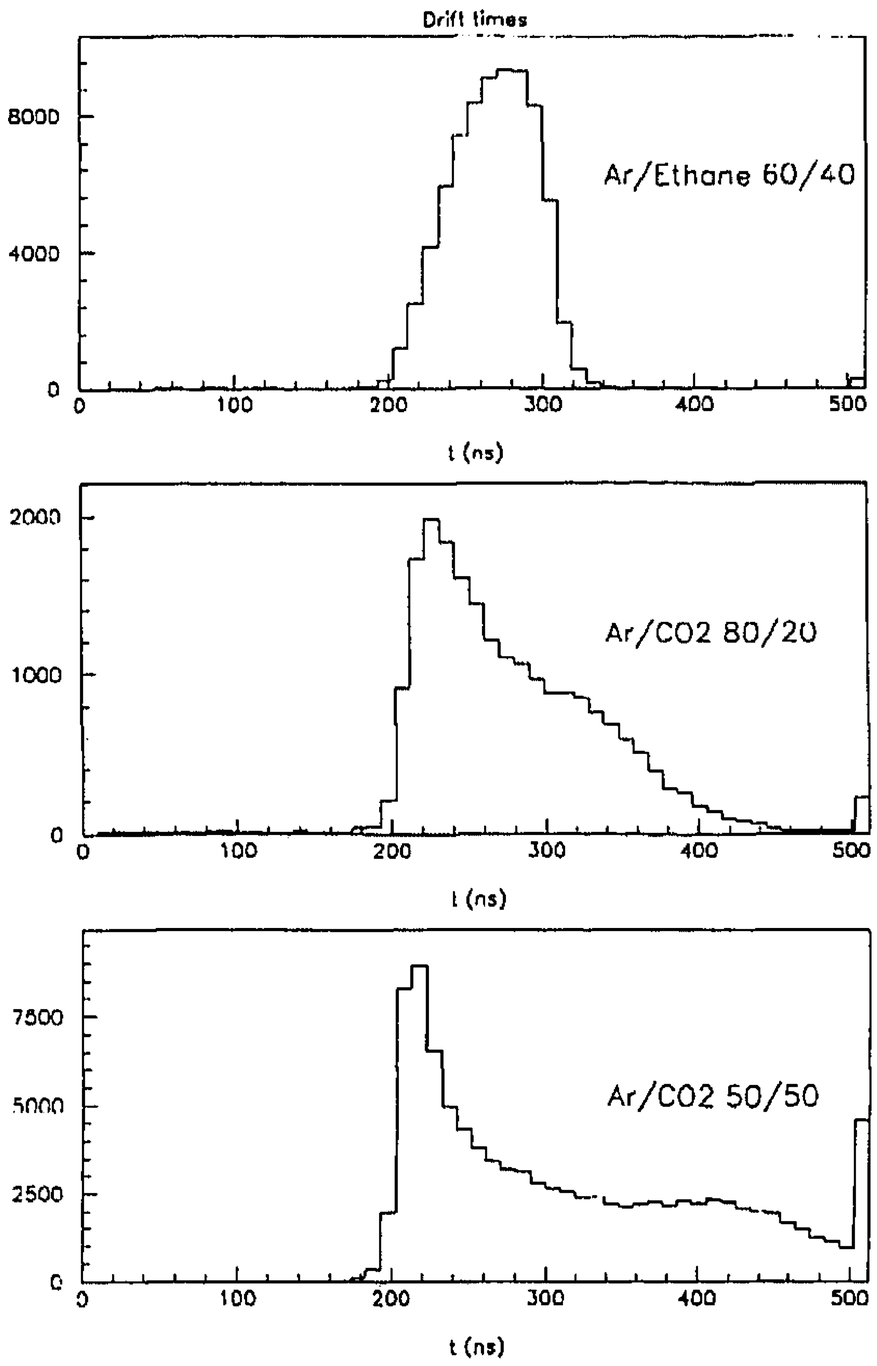


Fig. 12. Drift time spectra for three gas mixtures.

The ADC data was first corrected for pedestals. Then the correlated noise was corrected for by subtracting the average value of the ADC readings from strips at a sufficiently large distance from the track. For each plane the track position was calculated using only the three largest adjacent ADC values (see appendices A and C).

An attempt to measure differences in the gains of the preamplifier–ADC channels using test pulses on a wire failed. This was probably because of the too large differences in strips widths. The spread in gain of the preamplifier–ADC channels was smaller than 1% rms. If the gain of a preamplifier–ADC channel associated with strip $N$ is relatively high, then the positions of the measured tracks through the neighbouring strips $N-1$ and $N+1$ are "pulled" towards strip $N$. Using this effect and the data, the calibration factors of preamplifier–ADC channels were obtained by calculating residuals from track position spectra for each strip.

Using only 1000 events of perpendicular incident tracks, the relative alignment of the eight planes was obtained; the maximum deviation from perfect alignment was 150 μm. The relation between spatial resolu-

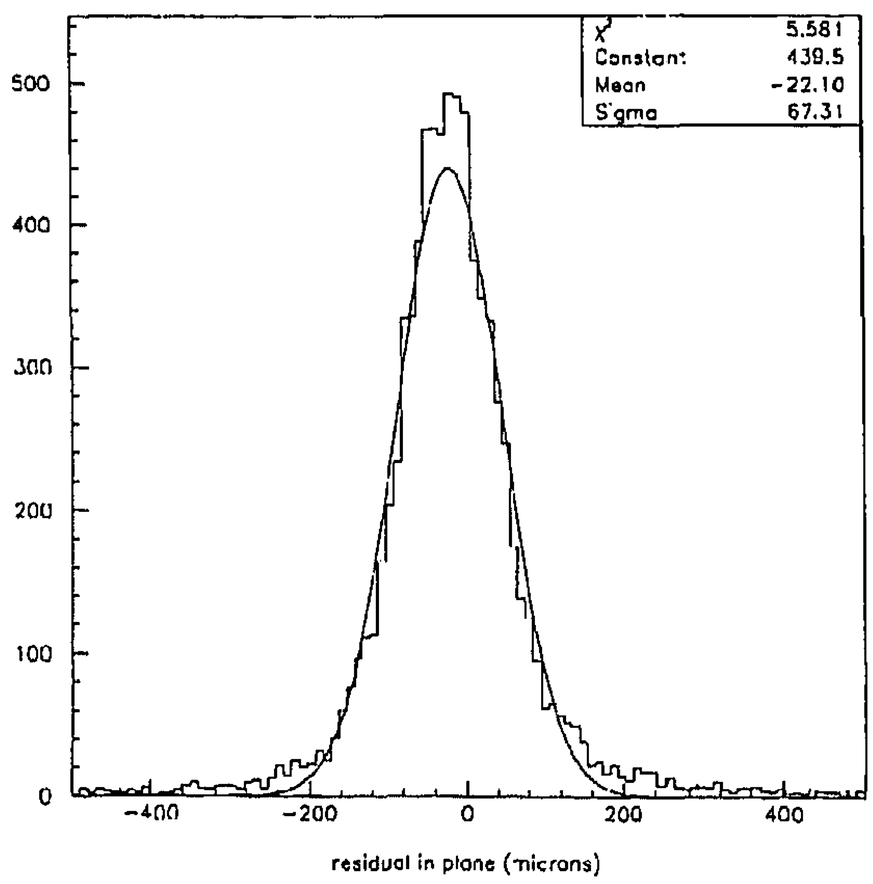


Fig. 13. Measured residual distribution of a prototype chamber layer. The corresponding spatial resolution is 64 μm. The drawn curve is a Gaussian fit.

tion and the width of the residual distribution was obtained by a Monte Carlo simulation.

Fig. 13 shows the spatial resolution of a single layer: the tails are larger than the fitted Gaussian curve. The large tails are partly in agreement with the Monte Carlo results. Fig. 14 shows results for two gases in the absence of a magnetic field: the performance of the chamber is the same for both gases. A fit to these results gives a value $\sigma_0 = 90$ μm for both gases. Some fine-tuned analyses of runs with small $\phi$ gave a value of 64 μm. This value was found to be independent of the $X$ coordinate; tracks passing the centre of a strip were measured with the same precision as tracks passing between two strips. This is in good agreement with Monte Carlo predictions. The parameter $\sigma_\phi$ is found to have a value of 1000 μm: this value is in reasonable agreement with the Monte Carlo result of 800 μm as showing in the top curve of fig. 14. The differences between measurements and predictions may be caused by correlated noise, by mechanical errors (the tolerances for the strip positions and strip width were 100 μm), by δ-ray emission by the foils or by an unknown effect. We note here that the width of the charge distribution over the strips increases with $\phi$; this was not taken into account. Fig. 15 shows the resolution per chamber plane in a magnetic field. The Lorentz angle shift is clearly visible. The fit parameters are the same as in fig. 14, indicating that the chamber performance is not affected by the magnetic field. A rotation of the chamber over the Lorentz angle around an axis parallel to the strips fully compensates the effect of a magnetic field.

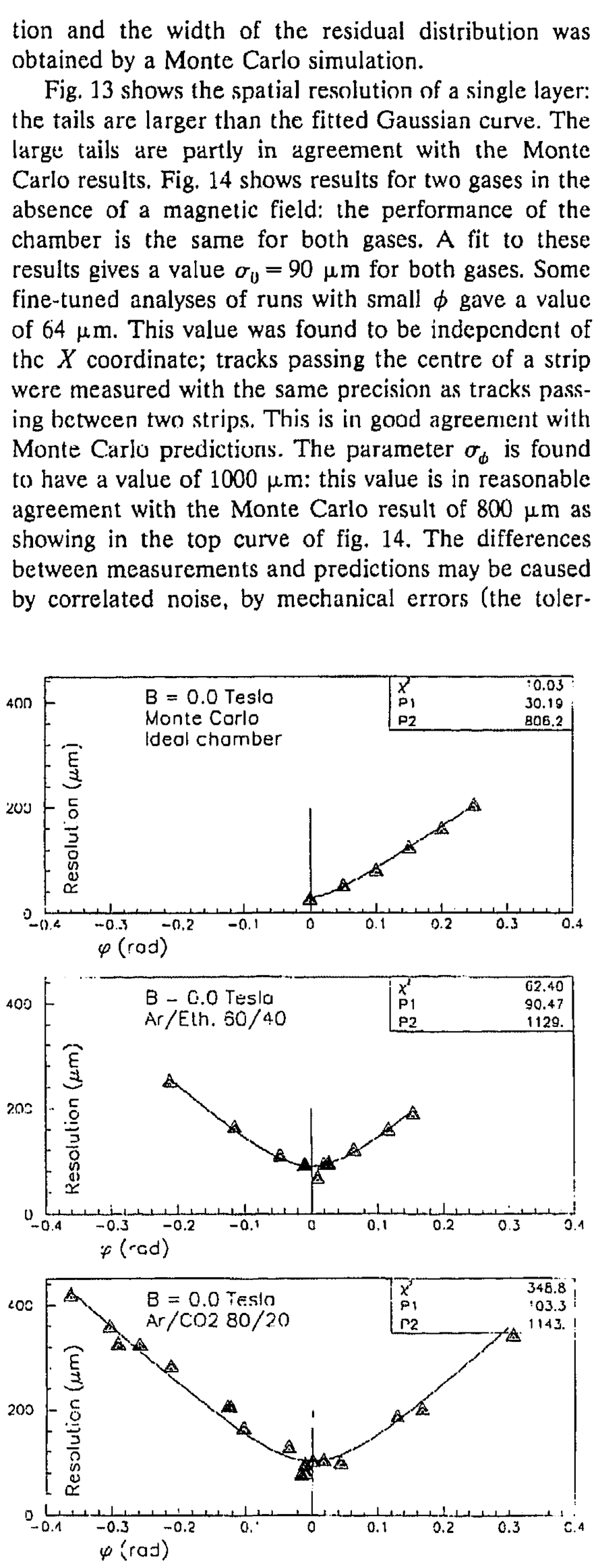


Fig. 14. Spatial resolution of prototype chamber as function of $\phi$, in the absence of a magnetic field. Top curve: Monte Carlo simulation for a mechanically perfect chamber including all processes mentioned.

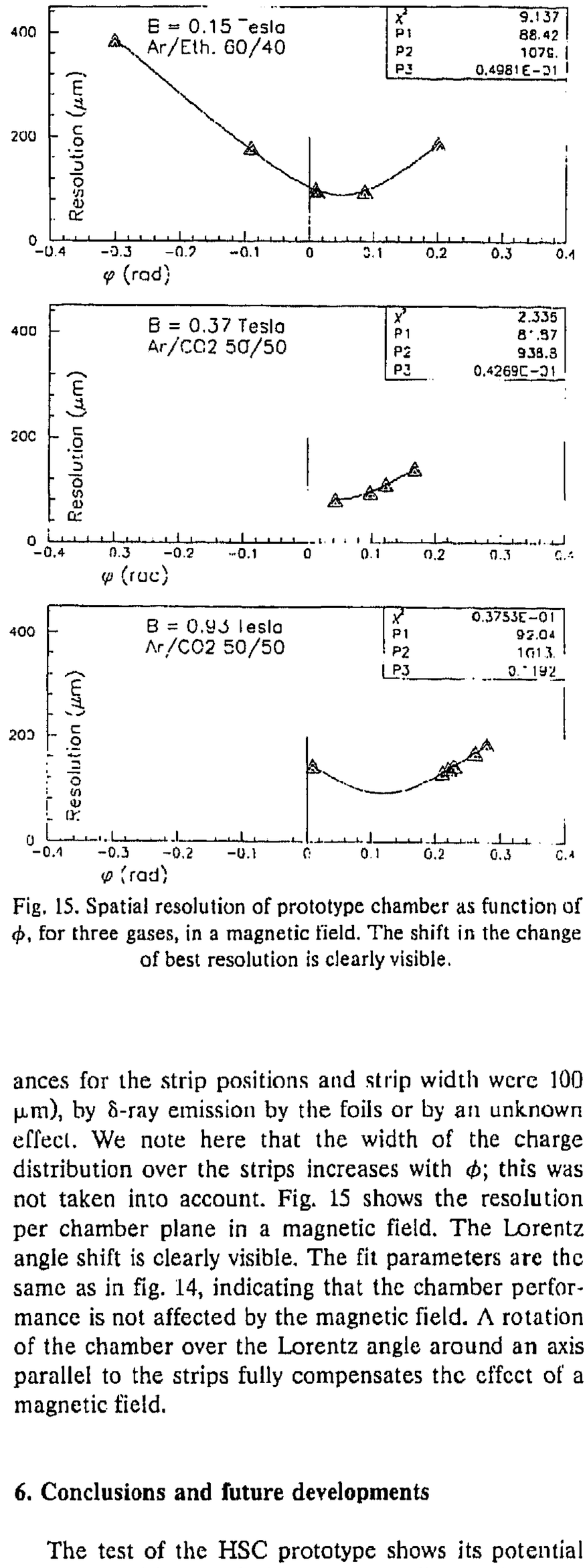


Fig. 15. Spatial resolution of prototype chamber as function of $\phi$, for three gases, in a magnetic field. The shift in the change of best resolution is clearly visible.

## 6. Conclusions and future developments

The test of the HSC prototype shows its potential for high position resolution: the degrading of the resolution with the angle of incidence was observed, as well as the influence of the magnetic field. The advantages

of HSCs, compared with conventional drift chambers are:

1) The chambers consist only of foils, wires, end covers and plastic plugs; these are all glued together in a jig.
2) Preamplifiers and discriminators are mounted next to the chamber edges. Since multiplexers can be used, the number of ADC channels can be reduced by a factor of at least 100. ADCs can be mounted on the chamber as well.
3) Two-dimensional, high precision readout is possible with one detector.
4) The weight of a HSC is low; its support structure can be simple. An inflatable version could be applied in space research.
5) The accuracy of one layer can be at least as good as 65 μm. In practice a value of 100 μm can be reached for the used geometry. The theoretical lower limit of the spatial resolution is determined by the diffusion of drifting electrons, and may be as low as 30 μm for Ar and 20 μm for Xe.
6) The chambers do not require tight tolerances in gas mixing ratio, gas temperature or gas pressure.
7) Magnetic fields do not cause a systematic error in the measured track position. The effects caused by the Lorentz angle can, if necessary, be eliminated by tilting the chamber.
8) The fast chamber response (the maximum drift time can be made smaller than 80 ns) makes it possible to derive a first level trigger signal.
9) Accurate data of the track position is available after 2 μs; this makes a second level trigger possible which has a good energy resolution.
10) A broken wire disables one layer at most. This will affect the spatial resolution only slightly.
11) There are no strong electric fields apart from the region of gas gain around the wire; stable operation with high gas gain is possible.

The essential drawback of HSCs is the degrading of the spatial resolution with increasing angle of incidence $\phi$. This effect can be limited by:

1) reducing the maximum angle of incidence $\phi$ by applying more chamber modules of smaller size;
2) using Xe gas instead or Ar;
3) increasing the gas pressure in the chamber;
4) decreasing the cell radius.

If the price of the front end electronics (preamplifiers, discriminators) can be of the order of 5 SF/channel, the costs of a muon detector built from honeycomb strip chambers is a factor of 5 less than comparable drift chambers. It would be attractive to build solid blocks of honeycomb planes which sample tracks every 10 mm. The track length can be decreased which is needed for a specific accuracy in the determination of muon momentum. This reduces the volume of the spectrometer magnet.

## 7. Future developments

The stability of foil under the influence of forces, humidity and temperature is being studied. Methods of obtaining foil with accurately positioned strips were evaluated. At present we use commercially available copper-sputtered mylar foil. By means of an endless rota-flexo printing process the strip images are applied to the foil using a special varnish. In an etching process the copper between the strips is removed. After this the varnish is removed. A machine has been constructed which folds long foils accurately; the foil width can be up to 1.5 m.

A low-noise charge amplifier for high source capacity has been developed, as well as a special 3-input discriminater which reacts if the middle input is carrying the largest signal and if the sum of the three inputs is larger than an external threshold (see appendix C).

In future tests we would like to study the ultimate spatial resolution, the drift times and the effects of electronegative gases. Special attention goes to the correlated and uncorrelated noise of the preamplifiers, as well as to current loops due to the virtual grounding of all wires and strips. The advantages of operation in the limited streamer mode will be investigated.

Monte Carlo simulations should determine the optimum cell radius for specific applications. Also the best values for other dimensions like the strip pitch and strip width should be calculated.

At present 25 monolayer honeycomb strip chambers are under construction for the tracking calorimeter TRACAL of the RD5 experimental site at CERN [24]. A new test chamber is foreseen to be constructed; it will have wires of 1 m, strips of 3 m and it should consist of 32 layers.

## Acknowledgements

We would like to thank Wim Gotink, Joost van Echtelt, Tjerk Lopik, Raymond Rosmalen, Hans Kok, Cees Brouwer, Robert Loos, Auke Korporaal and Hans Peter van der Kleij for various contributions. We thank the L3 Collaboration for the use of the L3 test beam site.

## Appendix A

*The charge distribution*

The charge on the wire and strips can be expressed in terms of the induced charge, due to a positive ion cloud, which drifts from the wire towards the cathode. The contributions of individual electrons created by the passing muon can be superimposed. The charge

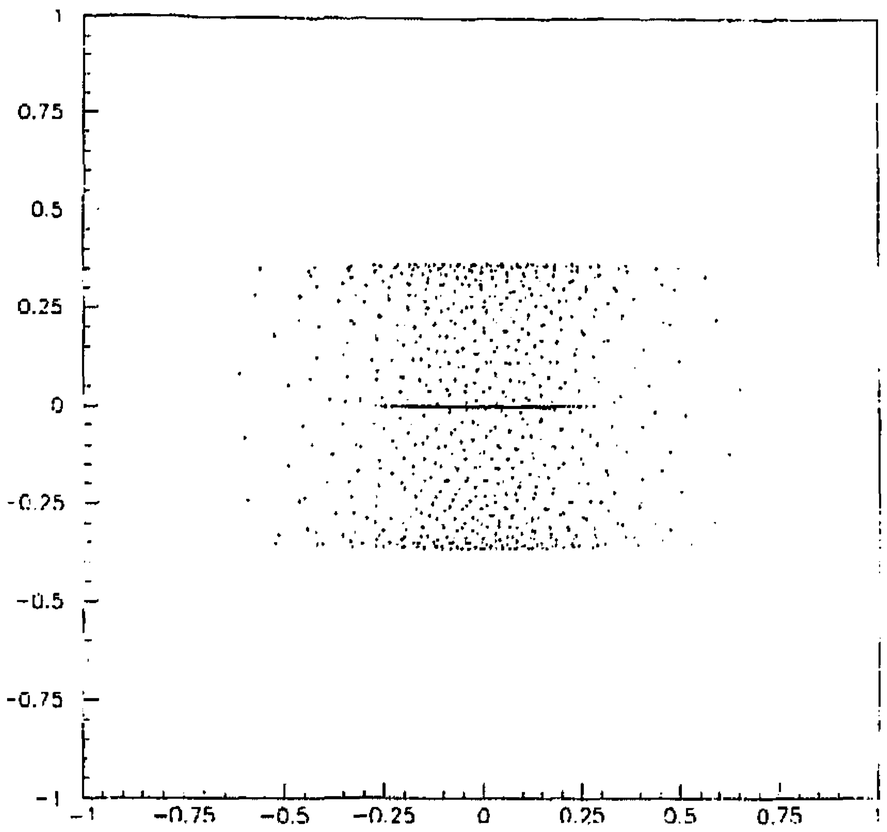


Fig. 16. Side view of the electrons on wire and tube. Note the regular patterns.

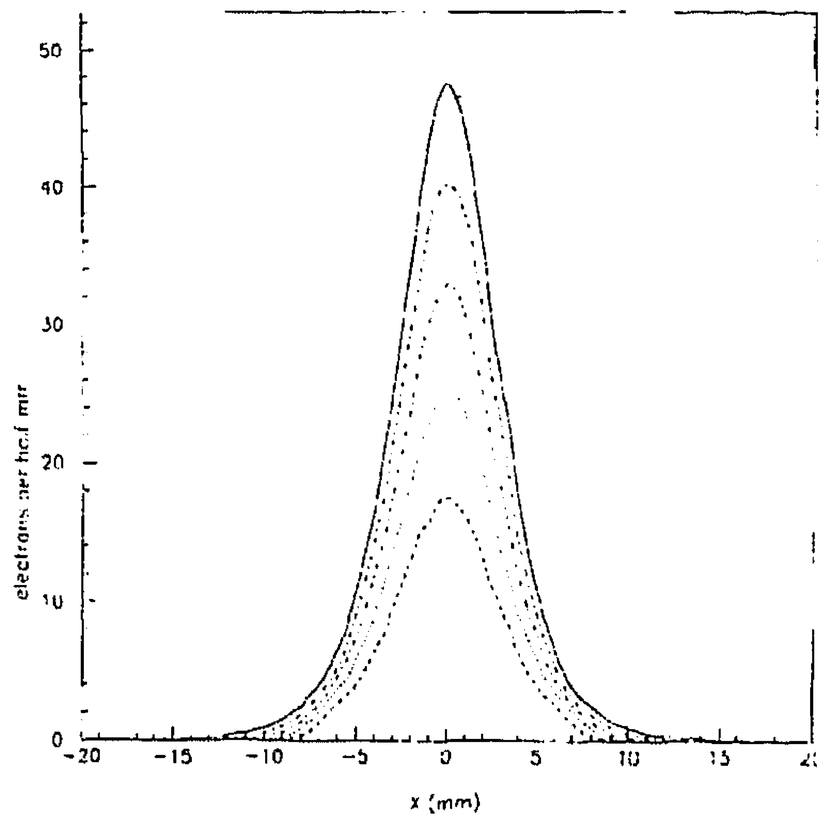


Fig. 18. The density of electrons on the cylindrical cathode of a counting tube as a function of the $X$ coordinate (direction along the wire). The curves show the distributions for $R_{cloud}$ = 50 (inner curve), 100, 200, 400 and 800 μm (outer curve). This correspond with ion drift times of 2, 8, 33, 130 and 520 ns, respectively.

distribution over the cathode strips was calculated using a multiparticle approach [14]. The number of participating electrons was 1000. The geometry of the hexagonal cell was simplified using a continuous cylindrical tube. The tube radius was taken as the average of the inner and outer radii of the hexagonal cell. Fig. 16 shows the electron distribution after equilibrium is reached. In this situation all the tangent components of the forces on the electrons are almost zero. The potentials of wire and tube, being the average of many potential "probes", are also zero. In fig. 17 the total charge on the cathode tube as a function of the distance between the ion cloud and the wire is shown. It demonstrates the accuracy of the method. Fig. 18 shows the distributions over the cathode tube for some values of the distance between the point-like ion cloud and the wire. The shape of the charge distribution depends somewhat on this distance. Given the integration time constant of the gated ADCs of 400 ns, the ions have a distance to the wire axis of approximately 0.8 mm. The outer curve of fig. 18 was used to obtain a numerical conversion of three charge signals to a centroid, relative to the strip center line.

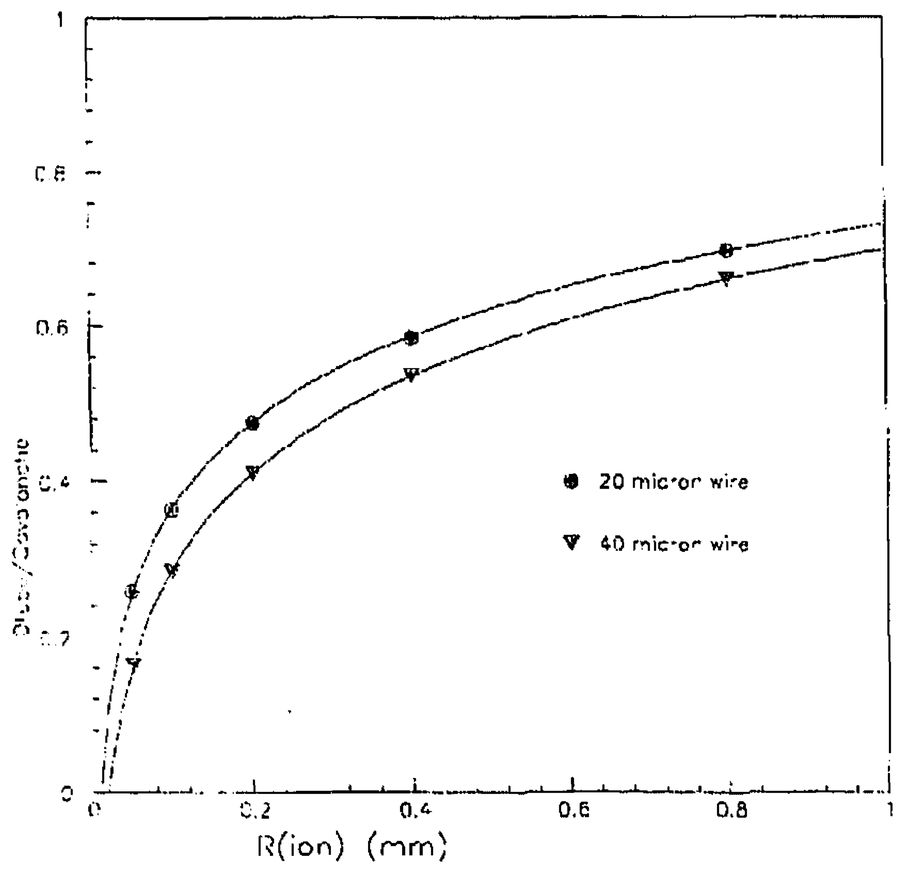


Fig. 17. The ratio of the total tube charge and the avalanche charge calculated as a function of the distance between the ion cloud and the wire axis. Drawn curve: analytical calculation. The values found with the multiparticle approach are accurate within 1 electrons, equivalent to 0.1%.

The charge distribution was parameterised by counting the electrons on three imaginary adjacent rings; the corresponding charges are called $Q_{left}$, $Q_{middle}$ and $Q_{right}$ respectively. The strip closest to the track carries $Q_{middle}$. In fig. 19 the ratio $Q_{right}/Q_{middle}$ is plotted versus the ratio $Q_{left}/Q_{middle}$, both for the calculation (fat dots and drawn curve) and for 1000 events with perpendicular tracks [10]. The X coordinate of a track is a function of the position of these points along the drawn curve. We approximated this function via angle $\alpha$, shown in fig. 19. The function

$$\alpha(x) = \mathrm{arctg}\left[\left(1 - \frac{Q_{right}}{Q_{middle}}\right) \Big/ \left(1 - \frac{Q_{left}}{Q_{middle}}\right)\right]$$

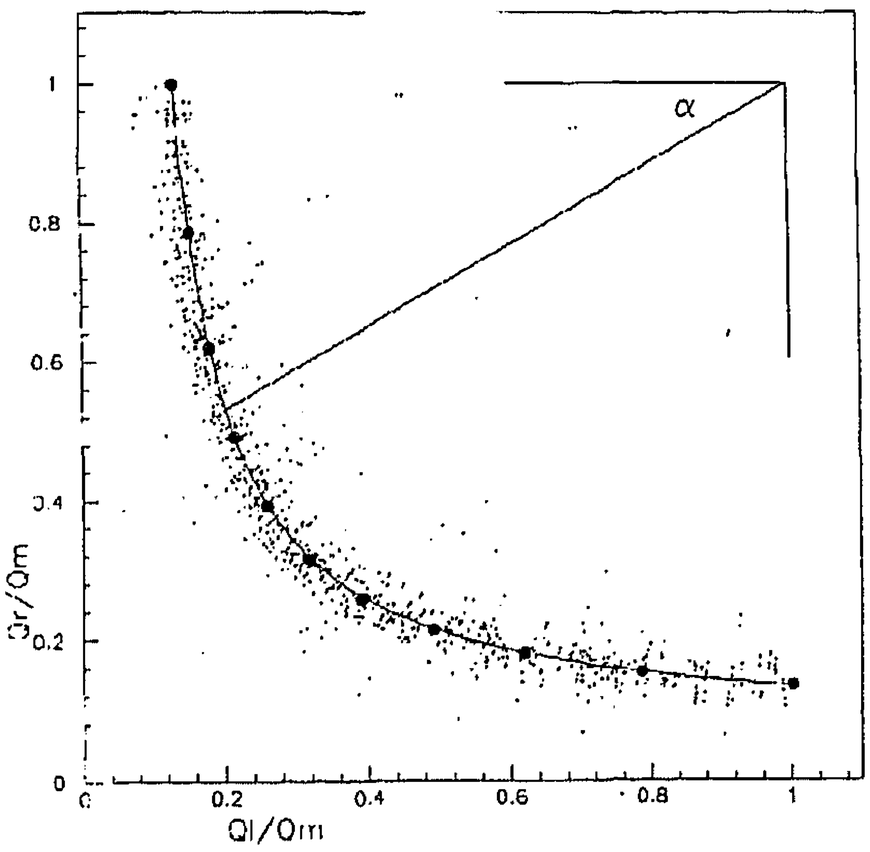


Fig. 19. The ratio $Q_{right}/Q_{middle}$ plotted versus $Q_{left}/Q_{middle}$. The $X$ coordinate of the track is a function of angle $\alpha$. The drawn curve is a fit through the thick points for $X = -2.5$ to $+2.5$ mm in steps of 0.5 mm which have been calculated using the multiparticle approximation. The dots are from real events measured with the prototype.

can now be calculated. The function

$$X_{cog} = 2.4065 \operatorname{arctg}\left(2.0995\left(\alpha - \tfrac{1}{4}\pi\right)\right)$$

was used in the analysis to calculate the centroid, relative to the centre of the strip carrying the largest signal.

## Appendix B

*Cell geometry*

The honeycomb structure of fig. 3 can be used as an alternative for straw tube chambers since it is easier to make and much more stable than an array of round tubes. In this case the foil can be either aluminised mylar, plain aluminium foil or plain copper foil without strips. In toroid magnetic fields the application of honeycomb strip chambers would require a complicated detector subdivision in order to keep the angle $\phi$ sufficiently small. In this case an accurate determination of the drift time would be more economical for the measurement of the track position. Honeycomb streamer tubes could be applied here.

In order to avoid the large capacitance between the upper and lower neighbouring strips, the full honeycomb structure could not be used for cathode readout; the layer-shifted geometry of fig. 4 was applied instead. The disadvantage of this geometry is that a single layer

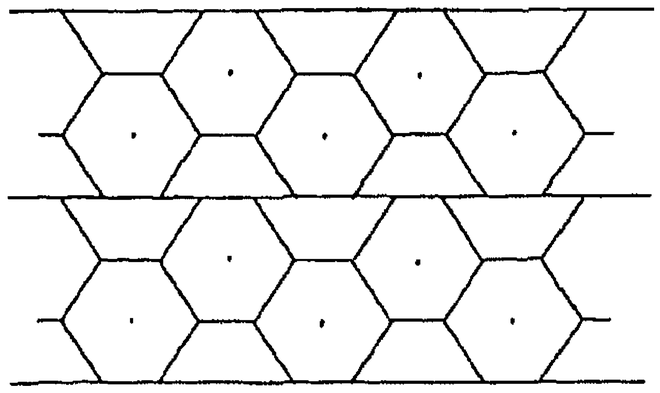

Fig. 20. Geometry with two fully efficient layers.

is not fully efficient due to the dead zone between two cells. Since an adjacent layer is shifted by half a cell pitch, two layers will form a fully efficient detector (except for tracks with the angle $\theta$ very close to 60°). For some applications where a full efficiency is obligatory the geometry of fig. 20 can be applied. The disadvantages, however, of such a geometry are: a) the chamber resolution may get worse because the constant $\sigma_\phi$, being roughly proportional to the effective layer thickness, is larger; and b) two adjacent wires may fire after different drift times; this may require complicated readout electronics (see appendix C).

The application of Kevlar fibres can cancel the thermal expansion of the foil.

The cell size is determined by the required position resolution per layer, the radiation density and the occupancy of the readout circuit. Technically, a cell radius of 1 mm is possible. This would allow the construction of a honeycomb chamber in areas with a radiation level of 100 Hz/mm$^2$. In large cosmic ray experiments chambers with a cell radius of 20 mm could be used as a low-cost replacement for scintillators.

## Appendix C

*Electronics and trigger for LHC applications*

In fig. 21 a low-cost readout for the strips is schematically shown. Each strip has its own low-noise preamplifier. The outputs of the preamplifiers are connected with a unit which detects the strip carrying the largest signal. This unit may consist of discriminators; the one which has the largest signal as input will flip first. Note that all strips signals have a common source; their timing is identical.

The output of the selector unit activates three analog switches in such a way that three lines are connected with the outputs of the preamplifiers closest to the track. An additional set of switches connects the signals $Q_{left}$, $Q_{middle}$ and $Q_{right}$ with their corresponding analog output lines. The signals are digitized by two FADCs applied in the divide mode, using the fact

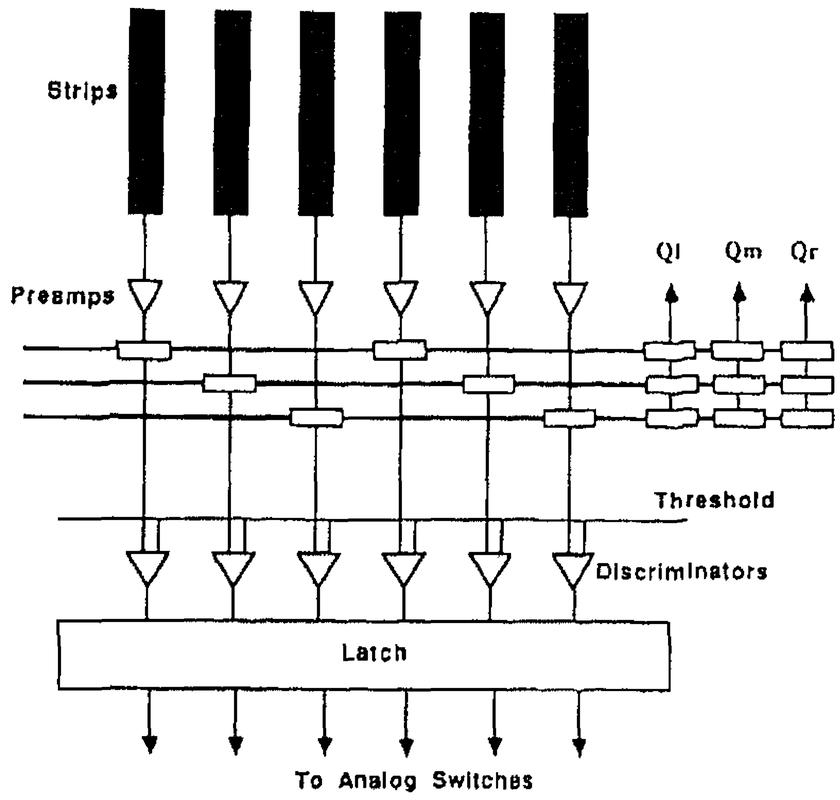


Fig. 21. Principle of the readout system of the strips. The multiplexer compresses, for example, 128 strips channel to one FADC system.

that $Q_{middle}$ is always the largest of the three. The ADC outputs are $Q_{left}/Q_{middle}$ and $Q_{right}/Q_{middle}$, respectively. In this way the main electronic readout circuit is reduced to a preamplifier, a discriminator and an analog switch per strip and two FADCs per chamber layer [25]. Two coincident tracks within a chamber layer can be recognized and processed by using some additional electronics. The strip preamplifiers and switches can be integrated in hybrids or ASICs, while the FADCs can be mounted elsewhere on the chamber.

The wires can be equipped with a preamplifier and a discriminator; by means of a priority encoder a hit wire per layer would be identified. By referring the timing of the hit for each chamber layer to the LHC/SSC machine clock, the $Z$ and $\theta$ coordinates can be computed as well as the timing of the p–p bunch in which the muon was created.

A trigger can be derived from the wire signals: they occur within the maximum drift time of 50–250 ns (depending on the gas mixture, chamber geometry and HV). A track trigger could consist simply of majority logic which responds if, for instance, at least half of the number of layers had a hit wire. The first level trigger uses the "hit wire" information of some layers. An algorithm which detects vertex pointing tracks would take 150 ns: the trigger can therefore be generated 200–400 ns after the bunch crossing. The first level trigger initiates an on-board transputer to readout the strip ADC and wire timing information. The transputer converts the strip ADC data into accurate track coordinates using lookup tables. After communication with the transputers associated with all the chambers in the sector of the experiment, the track curvature can be calculated and the second level trigger can be generated.

Communication between the chamber and the counting room would only require an optical fibre connection with the transputer on the chambers. This would reduce the cabling of the experiment by a large factor.

## References

[1] M. Pimiä et al., ECFA Large Hadron Colider Workshop, Aachen, October 1990, CERN 90-10, ECFA 90-133, vol. 3 (1990) p. 547.
[2] F. Bergsma et al. (LAA Large Area Devices Group), ibid., p. 489.
[3] K. Freudenreich et al., ibid., p. 791.
[4] The L3 Collaboration, Nucl. Instr. and Meth. A277 (1989) 187.
[5] R. Santonico and R. Cardarelli, Nucl. Instr. and Meth. 187 (1981) 377.
[6] H. van der Graaf et al., Proc. ECFA Study Week on Instrumentation Technology for High-Luminosity Hadron Colliders, Barcelona, 14–21 September 1989, CERN 89-10, ECFA 89-124, vol. 2 (1989) p. 441.
[7] H. van der Graaf et al., Proc. ECFA Large Hadron Colider Workshop, Aachen, October 1990, CERN 90-10, ECFA 90-133, vol. 3 (1990) p. 498.
[8] G. Charpak et al., Nucl. Instr. and Meth. 148 (1978) 471.
[9] E. Gatti and A. Longoni, R.A. Boie and V. Radeka, Nucl. Instr. and Meth. 188 (1981) 327.
[10] J. Chiba et al., Nucl. Instr. and Meth. 206 (1983) 451.
[11] J.S. Gordon and E. Mathieson, Nucl. Instr. and Meth. 227 (1984) 267.
[12] E. Mathieson and J.S. Gordon, Nucl. Instr. and Meth. 227 (1984) 277.
[13] E. Mathieson, Nucl. Instr. and Meth. 159 (1979) 29.
[14] H. van der Graaf and J.P. Wagenaar, Nucl. Instr. and Meth. A252 (1986) 311.
[15] V.C. Ermilova, L.P. Kotenko and G.I. Merzon, Nucl. Instr. and Meth. 145 (1977) 555.
[16] H. Fischle, J. Heintze and B. Schmidt, Nucl. Instr. and Meth. A301 (1991) 202.
[17] L. Katz and A. Penfold, Rev. Mod. Phys. 24 (1952) 28.
[18] G.D. Alkhazow, Nucl. Instr. and Meth. 89 (1970) 155.
[19] E.J. Kobetich and R. Katz, Phys. Rev. 170 (1968) p. 391.
[20] V. Palladino and B. Sadoulet, Nucl. Instr. and Meth. 128 (1975) 323.
[21] E. Gatti et al., Nucl. Instr. and Meth. 163 (1979) 83.
[22] I. Endo et al., Nucl. Instr. and Meth. 188 (1981) 51.
[23] P.R. Rewiersma, Internal documentation EA, NH 19-6112/NH 27-3262 (NIKHEF-H, Amsterdam, 1986).
[24] CERN/DRDC/90-36/P7 (CERN, Geneva, Switzerland, 1990).
[25] H. v.d. Graaf and J.P. Wagenaar, Nucl. Instr. and Meth. 217 (1983) 357.